ADVANCED MATERIALS
www.advmat.de

Dense All-Electrochem-Active Electrodes for All-Solid-State Lithium Batteries

Meiying Li, Tao Liu, Zhe Shi, Weijiang Xue, Yong-sheng Hu, Hong Li, Xuejie Huang, Ju Li, Liumin Suo,* and Liquan Chen*

The energy density presents the core competitiveness of lithium (Li)-ion batteries. In conventional Li-ion batteries, the utilization of the gravimetric/volumetric energy density at the electrode level is unsatisfactory (<84 wt% and <62 vol%, respectively) due to the existence of non-electrochemical active parts among the 3D porous electrodes, including electrolytes, binders, and carbon additives. These are regarded as indispensable and irreducible components of the electronic and ionic transport network. Here, a dense "all-electrochem-active" (AEA) electrode for all-solid-state Li batteries is proposed, which is entirely constructed from a family of superior mixed electronic–ionic-conducting cathodes, to minimize the energy density gap between the accessible and theoretical energy density at the electrode level. Furthermore, with the ionic–electronic-conductive network self-supported from the AEA cathode, the dense hybrid sulfur (S)-based AEA electrode exhibits a high compacted filling rate of 91.8%, which indicates a high energy density of 777 W h kg^{-1} and 1945 W h L^{-1} at the electrode level based on the total cathodes and anodes when at 70 °C.

1. Introduction

The pursuit of high energy density and a safe working process remains a topic of interest in the field of energy storage devices. Following a lengthy competition, lithium (Li)-ion batteries have come to dominate almost all the critical applications, including consumer electronic devices, electric transportation, and electric grid energy storage.[1,2] Compared with the early Li-ion batteries produced by Sony in the 1990s (80 W h kg^{-1}, 200 W h L^{-1} [$LiCoO_2$/C]),[3] the energy densities of the state-of-the-art Li-ion batteries have increased more than threefold (≈300 W h kg^{-1} [NCM811/Si–C], ≈700 W h L^{-1} [$LiCoO_2$/C]).[4,5] However, it is alarming that the energy density of the current type Li-ion batteries is very close to the limit.[6] The energy density at the electrode level is not only determined by the theoretical energy density of the electrochemical couples (energy density = average voltage × specific capacity) but is also highly sensitive to the weight fraction of the inactive components.[7,8] In addition, the binder and any conductive additives, especially the filling electrolyte, not only limit the energy density but also involve various security issues. As such, a number of research studies and technologies have been aimed at reducing the fraction of the inactive mass or volume; however, the attendant strategy is, at best, borderline.

In fact, only one case overcomes this barrier, that is, the Li metal anode. The absence of inactive additives and the high energy density ($Li^0 \rightarrow Li^+ + e^-$, 3860 mA h g^{-1}, 2061 mA h L^{-1}) ensure it is a prominent representative electrode.[9,10] In fact, the Li metal anode can be regarded as an "all-electrochem-active" (AEA) anode. However, on the cathode side, the realization of an AEA is primarily limited by its insufficient electronic conductivity (10^{-4}–10^{-10} S cm^{-1}), which is over five orders of magnitude lower than the conductive carbon black (≈10 S cm^{-1}),[11,12] and its sluggish Li-ion diffusion coefficiency (D_{Li}) (10^{-10}–10^{-15} cm^2 s^{-1}) that is much smaller than the liquid 1 M $LiPF_6$ in dimethyl carbonate–ethylene carbonate electrolytes (≈2×10^{-6} cm^2 s^{-1}).[13,14] To guarantee a well interconnected electronic–ionic network, the porous 3D electrode structure of the traditional Li-ion cathode must be uniformly filled with the conductive additive (carbon black), the polymer binder, and the liquid electrolytes, the total weight and volume fractions of which are >10 wt% and >30 vol%, respectively[15–17] (see the detailed information in Tables S1 and S2, Supporting Information).

The equivalent specific capacity ($ESC = C/m_{electrode}$, C is the capacity of the cathode and $m_{electrode} = m_{cathode} + m_{binder} +$

Dr. M. Li, Dr. T. Liu, Prof. Y.-s. Hu, Prof. H. Li, Prof. X. Huang, Prof. L. Suo, Prof. L. Chen
Beijing Advanced Innovation Center for Materials Genome Engineering
Key Laboratory for Renewable Energy
Beijing Key Laboratory for New Energy Material and Devices
Beijing National Laboratory for Condensed Matter Physics
Institute of Physics
Chinese Academy of Science
Beijing 100190, China
E-mail: suoliumin@iphy.ac.cn

Dr. M. Li, Prof. L. Suo
Center of Materials Science and Optoelectronics Engineering
University of Chinese Academy of Sciences
Beijing 100049, China

Dr. Z. Shi, Dr. W. Xue, Prof. J. Li
Department of Nuclear Science and Engineering and
Department of Materials Science and Engineering
Massachusetts Institute of Technology
Cambridge, MA 02139, USA
E-mail: liju@mit.edu

Prof. L. Suo
Yangtze River Delta Physics Research Center Co. Ltd
Liyang 213300, China

The ORCID identification number(s) for the author(s) of this article can be found under https://doi.org/10.1002/adma.202008723.

DOI: 10.1002/adma.202008723

$m_{\text{electrolyte-in-the-electrode}} + m_{\text{conductive-additive}}$) is defined to assess the capacity of the electrode, accounting for the overall impacts of the active cathode and the non-active parts, including the binder, carbon black, and electrolyte filling in the electrode. Based on the *ESC*, we can obtain the energy density of the electrode ($EG_{\text{electrode}} = ESC \times V$, where V is the discharge voltage). This indicates that the above compromises dilute the electrode-level energy density by at least 16%. Compared with the liquid-electrolyte-based electrode, the solid-state electrolyte (SSE)-based electrodes perform better in terms of security; however, perhaps unsurprisingly, they exhibit a lower $ESC_{\text{electrode}}$ due to their higher densities (oxide-based electrolyte: 2.93–5.07 g cm^{-3}, sulfide (S)-based electrolytes: 1.87–1.97 g cm^{-3}, PEO-based: 1.2–1.25 g cm^{-3}) and far more SSEs are required to ensure physical contact.[18,19] According to the existing data,[20–22] the weight fraction of cathode materials in all-solid-state Li batteries (ASSLBs) is less than 80 wt% (**Figure 1**d,e, see the detailed information in Tables S1–S3, Supporting Information), which results in low $ESC_{\text{electrode}}$ (0.8 × specific capacity) for this type of battery. In ASSLBs, it is theoretically possible to achieve an AEA electrode if the Li-containing cathode has high enough ionic and electronic conductivity, where the electrode is 100% occupied by active cathode materials and the Li-ion and electron transportation is self-actuating (Figure 1c).

2. The Concept of AEA Electrodes

In conventional Li-ion cathodes, the Li-ions reach the cathode through the electrolyte and electrons from the external circuit to the cathode and react at the three-phase interface (carbon/electrolyte/electroactive mass).[23,24] However, it is significant that the Li-ion and electron transportation self-relies on the all-in-one active electrode in our proposed AEA electrodes, the weight and volume percentages of which can increase to 100% and 89% (porosity 11%), respectively, in the electrode. To realize our idea, the ideal AEA candidates should have fast Li-ion transportability (alternative to electrolyte), high electronic conductivity (alternative to the conductive additive), and abundant Li storage sites (electrochemical active capacity). Furthermore, the ideal candidate would have a stable fixing structure with a low fluctuation of ionic and electronic conductivity that varies according to Li-ion concentration.

Following careful screening, a series of conductive transition metal sulfides caught our attention.[25–28] In previous works, pure amorphous transition metal sulfide cathodes were used as the electrode ASSLBs.[29–31] However, their electronic conductivity (≈10^{-3} S cm^{-1}) is four orders of magnitude lower than carbon (≈10 S cm^{-1}),[32] and their ionic conductivity is not particularly stable during the charge–discharge process. In our work, we selected crystal transition metal sulfides,

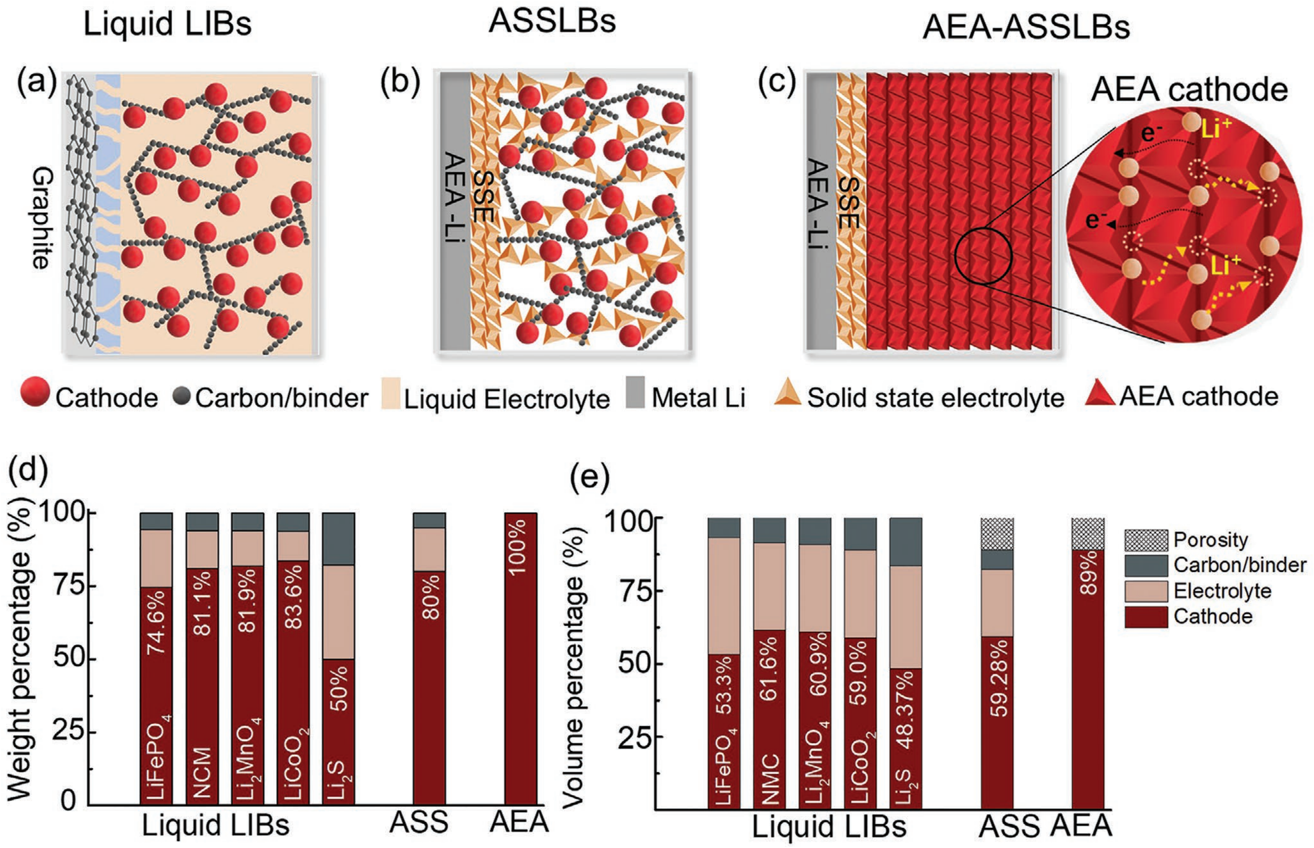

Figure 1. a–c) The concept of AEA electrodes: a) Commercial liquid Li-ion batteries (74.6–83.6 wt% cathode, anode: graphite); b) conventional ASSLBs (80 wt% cathode, anode: Li metal); c) the proposed AEA-ASSLBs (100 wt% AEA cathode, anode: Li metal). d,e) Summaries of the weight and volume percentages of various components.

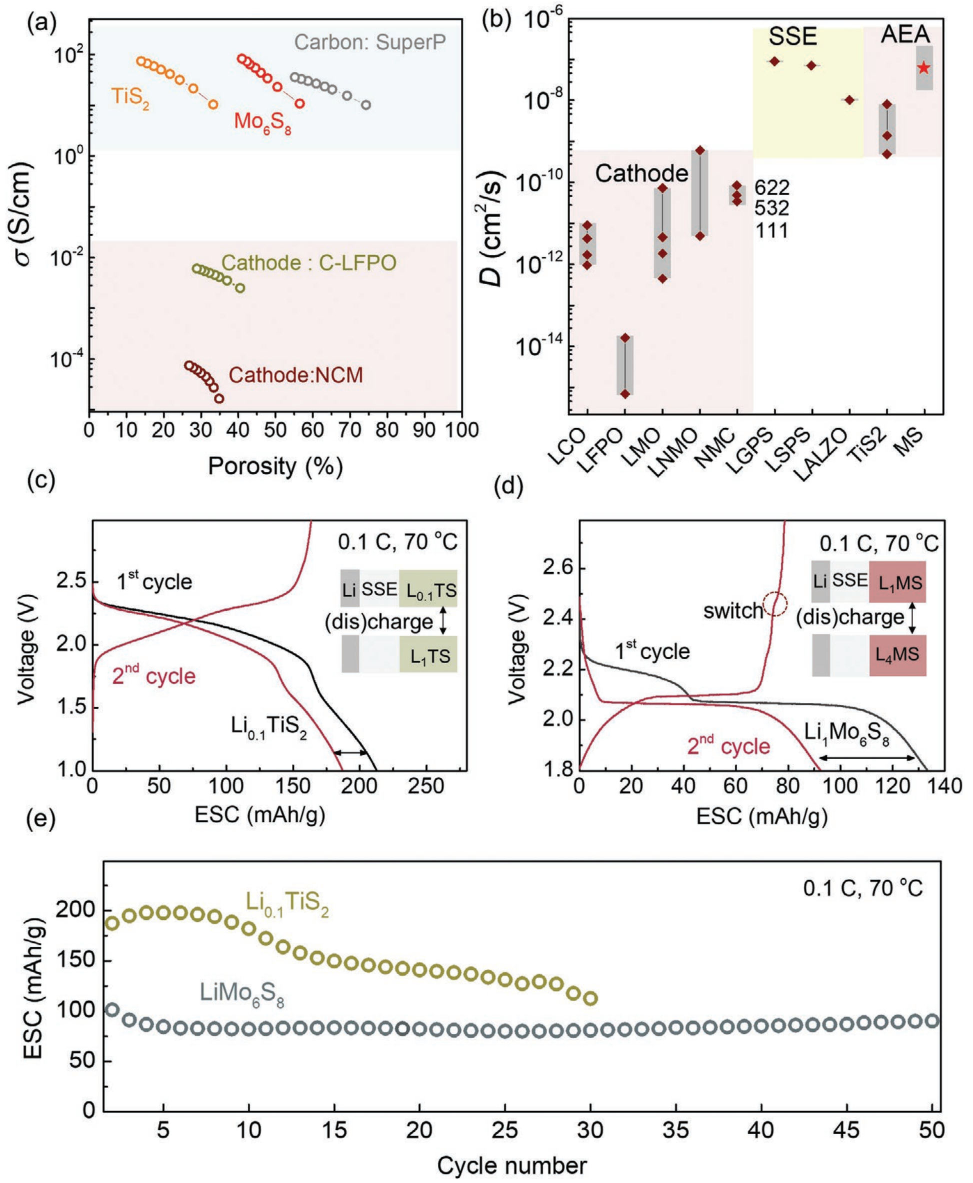

Figure 2. The proof-of-concept of the AEA-ASSLBs: a) Electronic conductivities of our AEA materials in comparison with the available conductive carbon additives and traditional cathodes, obtained via the 4-electrode powder electronic conductivity test. b) Li-ion diffusion coefficients of our AEA materials obtained via the potentiostatic intermittent titration technique method in comparison with the available traditional cathodes and typical SSEs. c,d) The galvanostatic discharge–charge profiles of the Li$_{0.1}$TiS$_2$- and LiMo$_6$S$_8$-based AEA cathodes. e) Their corresponding cycling stabilities at 0.1C/70 °C.

namely, layer-structured TiS$_2$ and chevrel-phase Mo$_6$S$_8$, which not only have a very stable host structure but also high electronic conductivity.[33] Mo$_6$S$_8$ and TiS$_2$ have a high electronic conductivity, which is over 3–6 orders of magnitude higher than that of the typical cathode materials (NMC532 and carbon-coated LiFePO$_4$), and comparable to the commercial conductive carbon (Super P) (**Figure 2**a, see the detailed information in Table S4, Supporting Information). These superhigh electronically conducting TiS$_2$ and Mo$_6$S$_8$ materials allow for eliminating the conductive carbon in the electrode. In addition, Mo$_6$S$_8$ and TiS$_2$ have a high Li-ion diffusion coefficient of $1.8–9.8 \times 10^{-8}$ and 8×10^{-9} to 9×10^{-10} cm^2 s^{-1} (see the detailed information in Figure S1, Supporting Information),[25,34,35] which is comparable to that of SSEs (Li$_{10}$GeP$_2$S$_{12}$, $8.8–9 \times 10^{-8}$ cm^2 s^{-1}, Li$_{10}$SiP$_2$S$_{12}$, $7–7.2 \times 10^{-8}$ cm^2 s^{-1}, Li$_{6.25}$Al$_{0.25}$La$_3$Zr$_2$O$_{12}$, $1–1.1 \times 10^{-8}$ cm^2 s^{-1}), and far higher than that of the conventional commercial cathodes (LiFePO$_4$: 6.8×10^{-16} to 1.8×10^{-14} cm^2 s^{-1}, NMC: $2.8–8 \times 10^{-11}$ cm^2 s^{-1}, LiCoO$_2$: 10^{-11} to 10^{-12} cm^2 s^{-1}) (Figure 2b, see the detailed information in Table S5, Supporting Information).[36–45] As such, they can serve as solid-state electrolytes rather than filling electrolytes in the electrodes. Meanwhile, the intercalation compounds of Mo$_6$S$_8$ and TiS$_2$ enable Li-ion storage in their host with the high stability of the host framework structure and the low fluctuation of ionic and electronic conductivity. Based on the above merits of the physicochemical properties, we decided to use full electrochemical active electrodes (100% Mo_6S_8 or TiS_2 cathode and Li metal anode) to construct an ASSLB.

3. Demonstration of AEA All-Solid-State Li-Batteries

To provide a proof-of-concept, AEA-ASSLBs were constructed using a configuration of AEA cathode (100% TiS_2 or Mo_6S_8)/SSEs ($Li_{10}GeP_2S_{12}$–Li_3PS_4)/AEA anode (100% Li metal anode).[46] As shown in Figure 2c,d, the TiS_2-based AEA-ASSLBs had an initial discharge capacity of 213 mA h g^{-1} at 70 °C, with the characteristic smooth slope in the voltage profile demonstrating the solid-solution reaction. Meanwhile, the Mo_6S_8-based AEA-ASSLBs delivered a capacity of 130 mA h g^{-1}, with two characteristic well-defined plateaus in the voltage profile corresponding with the two-phase reaction (2.3 V, $Mo_6S_8 \rightarrow LiMo_6S_8$, and 2.05 V, $LiMo_6S_8 \rightarrow Li_3Mo_6S_8/Li_4Mo_6S_8$) (Figure 2d). Since both pristine TiS_2 and Mo_6S_8 are Li-free, a partial pre-lithiation was required to provide the function of a Li-ion conductor on the initial discharge. Specifically, the observed capacity gap between the first and second discharge roughly correlates with the Li consumption of the pre-lithiation process corresponding with $Li_{0.1}TiS_2$ (LTS) (25 mA h g^{-1}) and $LiMo_6S_8$ (LMS) (35 mA h g^{-1}). Starting with these very partially pre-lithiated materials (LTS and LMS), the batteries had a reversible capacity of more than 180 mA h g^{-1} for LTS and 90 mA h g^{-1} for LMS, demonstrating that our AEA-ASSLBs can work well based on both solid-solution (LTS) and two-phase reaction (LMS) mechanisms. In sharp contrast, the AEA electrode constructed using the typical $LiFePO_4$ and $Li_4Ti_5O_{12}$ materials failed (see the detailed information in Figure S2, Supporting Information). Compared with the LTS, the LMS exhibited better cycling stability with a high capacity retention of 89% after 50 cycles (compared with the 2nd cycle).

The aforementioned distinctions could be attributed to the materials' intrinsic physicochemical properties, crystal structure, and different Li storage mechanisms. LTS presents a solid-solution reaction involving Li-vacancy disorder, the Li-ion diffusion coefficient of which largely depends on the vacancy concentration and is susceptible to the Li concentration.[47] Upon cycling, any trapping Li for the irreversible capacity loss could potentially gradually lower the kinetic of the LTS–AEA electrode, resulting in capacity fade (Figure 2e). In contrast, LMS maintains a high D_{Li} with a very low fluctuation from 1.8×10^{-8} to 1.7×10^{-7} cm^2 s^{-1} (**Figure 3**a). The *C*-rate performance also

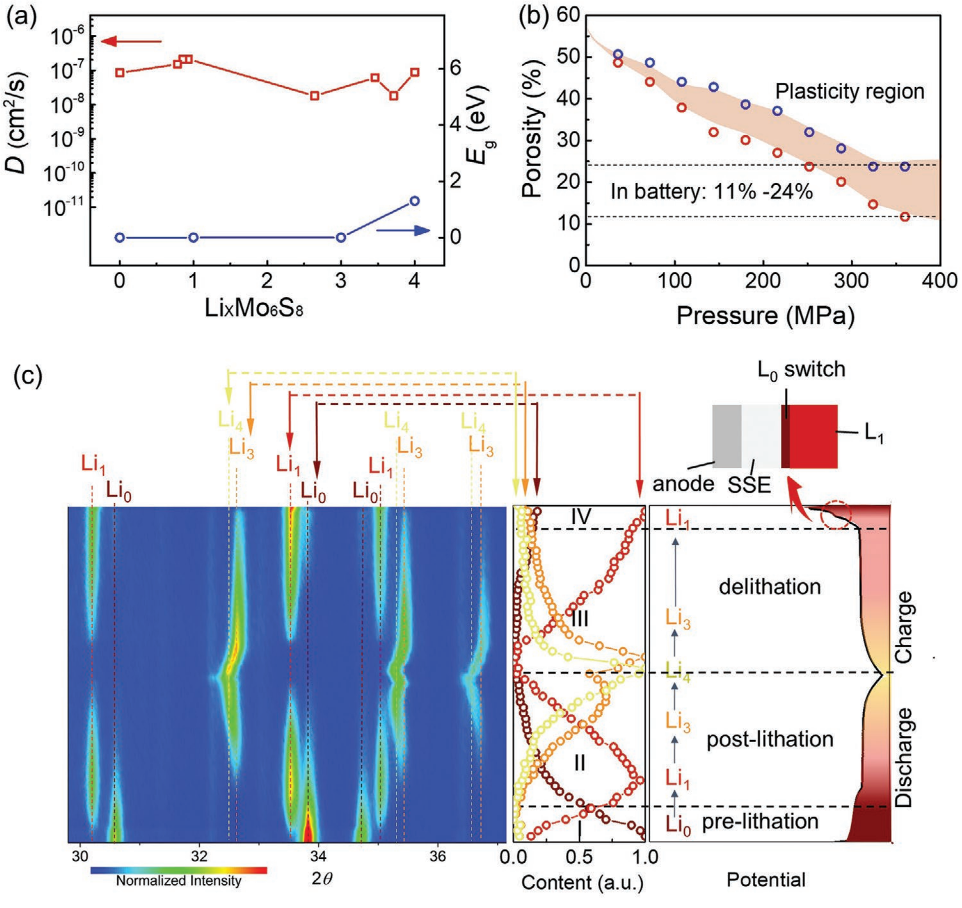

Figure 3. a,b) The electrochemical mechanism of the LMS-based AEA cathode: a) Li-ion diffusion coefficients and energy bandgap of $Li_xMo_6S_8$ ($x = 0$, 1, 3, 4), b) the porosity of the AEA Mo_6S_8 electrode as a function of the applied pressure. The red circles represent the value test with pressure and the blue ones represents the value test releasing the pressure. c) In situ XRD analysis of the LMS-based AEA cathode (left). The normalized intensity of the peak at 33.9° (Li_0), 33.7° (Li_1), and 32.7° ($Li_{3–4}$) in different stages (middle) and the phase transition process accompanying the charge–discharge profiles (right).

verified the fast kinetic of Li-ion transportation, and the LMS–AEA electrode with a high cathode mass loading of 13.91 mg cm^{-2} (compacting density is 4.5 g cm^{-3} and the thickness of electrode is 30.9 µm) eliminates the possibility that the capacity only originates from the interfacial electrochemical reaction between the LMS and the SSE (see the detailed information in Figures S3 and S4, Supporting Information). Furthermore, our LMS–AEA electrode exhibited superior plasticity, which enabled elastic recovery after releasing the pressure. As the apparent gap in porosity marked by the shadowed area in Figure 3b indicates, the porosity of Mo_6S_8 decreased to 11% under 360 MPa (the applied pressure of ASSLBs in real operating conditions) and rebounded to 24% after the pressure was released (see the detailed information in Tables S6 and S7, Supporting Information). The excellent deformability of the LMS–AEA electrode is not only favorable in terms of achieving a dense electrode and good physical solid–solid interfacial contact but is also helpful for buffering the volume expansion of cathode materials during cycling. Thus, in the following section, LMS is selected as our priority material.

To verify the phase transformation during charging, in situ X-ray diffraction (XRD) was performed for a tailor-made ASSLB (Figure 3c). The pristine electrode belongs to the Li_0 phase (Mo_6S_8) (JCPDC: 89–5114) with three major peaks at 30.7° $(12\bar{1})$, 33.9° $(21\bar{2})$, and 34.8° (104). At the initial stage of the discharge, a new Li_1 phase ($LiMo_6S_8$) [JCPDC: 81–0858, 30.4° $(12\bar{1})$, 33.7° $(21\bar{2})$, and 35.0° (104)] was generated along with a decrease in the intensity of the Li_0, indicating the two-phase transformation between Li_0 and Li_1. Subsequently, along with a second discharge plateau (2.05 V), the Li_1 phase further transformed into a Li_3 phase [JCPDS81-0859, 32.7° $(21\bar{2})$, 35.5°(104), and 36.8°(220)] and finally converted into $Li_4Mo_6S_8$ (L_4 phase) [JCPDS: 81–0860, 32.6° $(21\bar{2})$, 35.4° (104), and 36.7° (220)]. To further quantify the relative content of the different phases in the two-phase coexistence region, the normalized intensity based on the $(21\bar{2})$ peak was obtained, as shown in Figure 3d (middle). This revealed clear multiple two-phase coexistences that were consistent with the charge–discharge profiles (Figure 2d). The final discharge product of Li_4 can only be reversibly converted into Li_1 with a trace of Li_0 phase remaining that corresponds with the very short plateau at 2.45 V at the end of the charge stage (circled in Figure 3c, right). The LMS–AEA electrode processes a step-wise electrochemical reaction with the multiple phase transformations in the first cycle, which can be divided into four stages in the order of stage I, stage II, stage III, and stage IV (Figure 3c, middle). During stages I and II, the increase in Li concentration promotes Li-ion transportation in the AEA electrode due to the formation of $Li_xMo_6S_8$ (x = 1, 3, 4) with a high diffusion coefficient D_{Li}. The high Li concentration phases gradually transformed into low phases during delithiation (stage III) (Li_4–Li_3–Li_1). At the end of stage IV, an ionically blocking interphase layer mainly consisting of Li_0 formed since this is a Li-free and ionic-isolating phase, and its formation on the interface of the electrode–electrolyte shut down the further phase transformation from Li_1 to Li_0 in the bulk electrode, much like a specific "ionic switch." At this time, the delithiation process is blocked and Li_1 is retained to a large extent. These results confirmed our hypothesis that the LMS–AEA electrode requires an initial partial pre-lithiation such that its Li ionic and electronic conductivities are qualified.

Based on the above results and discussion, we have successfully demonstrated the proof-of-concept of the AEA electrode in ASSLBs. This AEA electrode can also work at room temperature (see the detailed information in Figures S5, Supporting Information). However, compared with conventional Li-ion batteries, the $ESC_{\mathrm{electrode}}$ of the LMS–AEA cathode was only 90 mA h g^{-1}, which means that it had not yet realized its full potential in terms of energy density. To further display the advantages of the AEA electrode, a hybrid S_8–Mo_6S_8 (S–LMS)-based AEA cathode was attempted, since an S cathode has a high theoretical capacity of 1,675 mA h g^{-1}, with redox potentials ideally below the "ionic switch" of 2.45 V.[48–51] Given that a S_8 cathode is electronically insulating, the conductive LMS served as an efficient electronically and ionically conducting network within the AEA electrode, with the weight percentages of S_8 and Mo_6S_8 32.5 and 67.5 wt%, respectively. The transmission electron microscopy (TEM) image of the hybrid S–LMS–AEA cathode (**Figure 4**a) revealed the coexistence of amorphous S_8 (marked by the yellow-block) and crystalline Mo_6S_8 (marked by the green lines), the electron diffraction patterns are shown in Figure S6, Supporting Information, and the XRD patterns are shown in Figure S7, Supporting Information. Inside the electrode, the small Mo_6S_8 nanosheets were mutually interconnected and thus constructed a conductive network for transport of electrons/ions. Furthermore, the amorphous S_8 was homogenously dispersed, which was reflected by the 10–30 nm nanodomain distributed in the Mo_6S_8 framework that guarantees the desired electrons/ions transport in the insulating S_8. Unlike conventional all-solid-state Li–S cathodes with three single-function materials (carbon/SSE/S) for forming three-phase reaction interfaces, our hybrid S–LMS–AEA cathode had an all-in-one ionically/electronically transporting two-phase reaction interface (LMS/S), which allows for avoiding the unbalanced transport between the electron (by carbon) and Li-ion (by the SSEs).

Figure 4b shows the cross-sectional images and the elemental mapping of the hybrid S–LMS–AEA cathode and the $Li_{10}GeP_2S_{12}$ SSE. The local element distribution of the phosphorus (P) indicated a pure AEA cathode electrode without any SSE component (see the detailed information in Figures S8–S10, Supporting Information), which was confirmed by the obtained energy-dispersive spectrum, as shown in Figure 4c. Furthermore, the volumetric density at the electrode level is highly dependent on the porosity, which can be reduced by applying pressure in ASSLBs. It is significant that our S–LMS–AEA electrode had a very high compacted filling rate of 91.8% at 360 MPa, which was due to the creep of the soft Mo_6S_8 and S_8 (Figures 3b and 4d, see the detailed information in Tables S6 and S8, Supporting Information), the 8.2% residual porosity of which allowed for accommodating the volume expansion. Combining the advantages of AEA electrodes in terms of *ESC*, the theoretical volumetric density of the S–LMS–AEA electrode was estimated to be above 3565.3 W h L^{-1} (in terms of the volume of the Mo_6S_8 and S_8), which is more than double that of the conventional S–C-LGPS (32.5 wt%, 17.5 wt%, 50 wt%) electrode with the same fraction of sulfur.

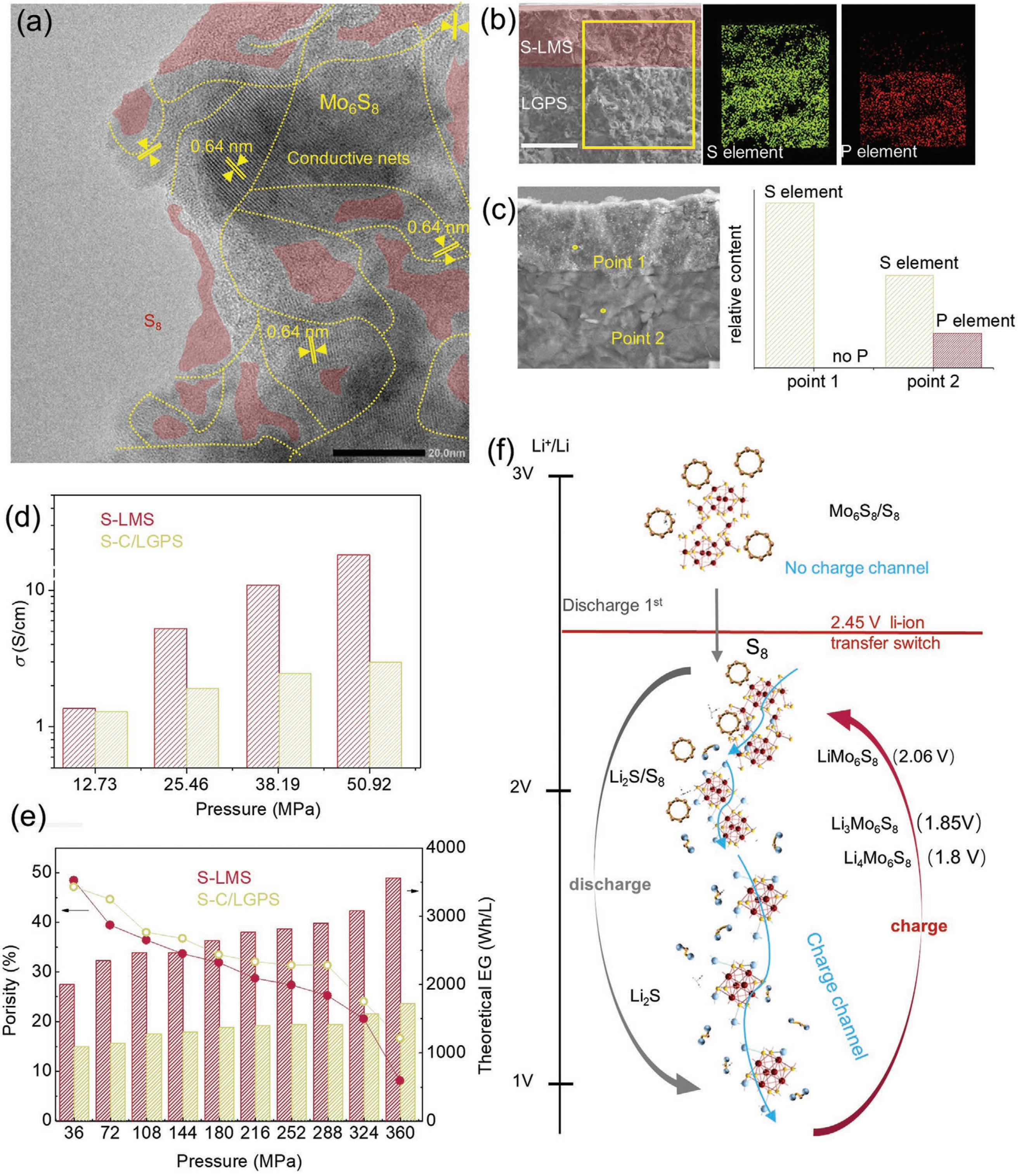

Figure 4. The structure and electrochemical mechanism of the hybrid S–LMS–AEA cathode (32.5%S_8–67.5%Mo_6S_8). a) TEM image of the S–LMS–AEA cathode. b) The cross-sectional SEM images of the AEA cathode/$Li_{10}GeP_2S_{12}$ interface with the energy dispersive spectrometer (EDS) mapping of the P and S elements. c) EDS point analysis of the P and S elements in the AEA cathode (Point 1) and the $Li_{10}GeP_2S_{12}$ (Point 2). The black scale in (a) is 20 nm, and the white scales in (b) and (c) are 50 µm. d,e) Comparison of the electronic conductivities, theoretical volumetric energy density, and porosity of the S–LMS–AEA cathode and those of a typical S–C–LGPS cathode (32.5 wt%, 17.5 wt%, 50 wt%, see the detailed information in Figure S11, Supporting Information). f) The electrochemical redox mechanism of the S–LMS–AEA cathode.

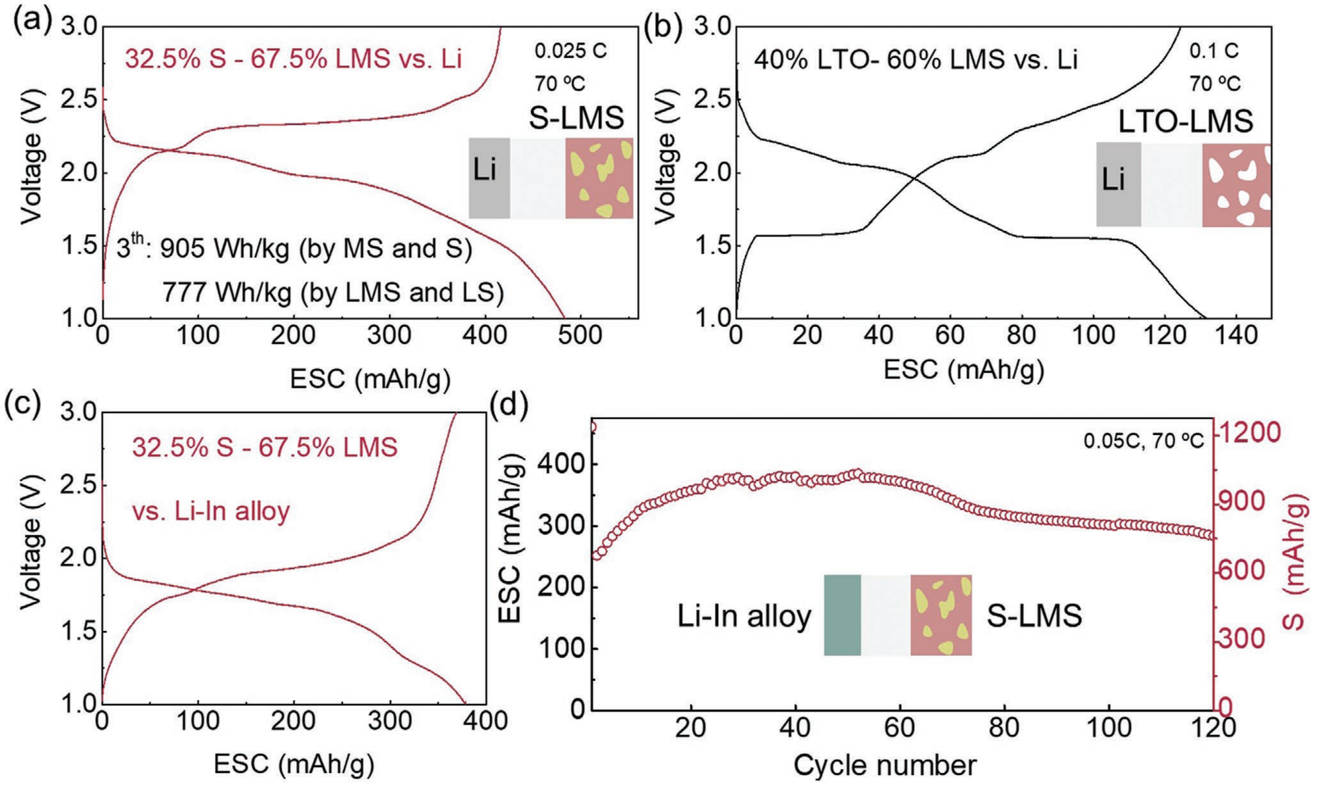

Figure 5. The strategies for high energy density AEA-ASSLBs. a–c) Typical charge–discharge profiles of ASSLBs with hybrid S–LMS (32.5% S_8–67.5% Mo_6S_8) versus Li, LTO–LMS (40% $Li_4Ti_5O_{12}$–60% Mo_6S_8) versus Li, and S–LMS versus Li–In alloy anode. d) Cycling stabilities of the AEA battery with the S–LMS cathode. The capacity was calculated based on the $ESC_{\text{electrode}}$.

As Figure 4f illustrates, we proposed a possible electrochemical mechanism for a hybrid S–LMS–AEA cathode. Below 2.45 V, the AEA Mo_6S_8 electrode was first pre-lithiated into LMS before it was reversibly transformed into the following Li-rich phases ($Li_1 \leftrightarrow Li_4$). Moreover, simultaneously, the S_8 cathode underwent a conversion of $S \leftrightarrow Li_2S$, delivering a specific capacity of 1,290 mA h g^{-1} (by the initial electrode mass, before discharge without Li). The $ESC_{\text{electrode}}$ was used instead of the specific capacity for the cathode to evaluate the energy density at the electrode level. In terms of the hybrid S–Mo_6S_8–AEA cathode with the Li metal, a high $ESC_{\text{electrode}}$ of 483 mA h g^{-1} (0.8 mA h cm^{-2}, the theoretical value is 630 mA h g^{-1}, supplementary material) was achieved after three cycles, with gravimetric and volumetric energy densities of 905.5 W h kg^{-1} and 2778 W h L^{-1}, respectively, at the electrode level, which was close to the theoretical energy density of 1260 W h kg^{-1} and 3865 W h L^{-1} (**Figure 5**a, see the detailed information in the Supplementary calculation model). Meanwhile, in terms of the discharge products, Li_2S and $Li_4Mo_6S_8$, the values were 777 W h kg^{-1} and 1945 W h L^{-1}, which is still higher than those of the commercial high-density $LiCoO_2$ electrode (476 W h kg^{-1}, 1698 W h L^{-1}, by the electrode mass) (see the detailed information in Table S8, Supporting Information). Furthermore, to demonstrate the cycling stability of our hybrid S–LMS–AEA cathode, a Li–In AEA anode was applied to stabilize the interface between the Li metal anode and the SSE. This demonstrated that our AEA ASSLBs had excellent cycling stability with a capacity retention of 76% after 120 cycles (compared to the 30th cycle with the highest energy density, Figure 5c,d).

Our hybrid S–LMS–AEA cathode exhibited the following significant advantages: 1) The electrodes were constructed using 100% electrochemically active substances without any inactive materials, thereby maximizing the cathode capacities at the electrode level. 2) The all-in-one electronic/ionic conductive network of the LMS cathode is favorable in terms of enhancing the electrode kinetic through avoiding the unbalance and inhomogeneous reaction at the three-phase reacting interfaces (carbon/electrolyte/S). 3) Both the AEA cathode and the SSEs belong to the sulfur family, which allows for excellent mutual compatibility through their high affinity. 4) The elastic nature of the AEA cathode alleviates the volume expansion of the S_8/Li_2S during cycling. In principle, the LMS–AEA cathode has strong universality, combined with other active materials with a redox potential of less than 2.45 V possible. For example, another type of hybrid AEA cathode with 40% $Li_4Ti_5O_{12}$ and 60% Mo_6S_8 (LTO–LMS) exhibited superior cycling stability, with an $ESC_{\text{electrode}}$ of 130 mA h g^{-1} at the electrode level (Figure 5b–d).

4. Conclusion

We have proposed a new concept of AEA all-SSE with a superior electronic/ionic mixing conductor as an alternative to carbon black and the electrolyte in the electrode. With consideration of our AEA principle and the screening criteria, the LTS- and

LMS-based AEA electrodes were selected due to their high electronic conductivity, high ionic diffusion coefficient, and stable Li-storage performance. In these AEA electrodes, the energy density gap at the electrode level between the accessible and the theoretical value is bridged and minimized as far as possible. More significantly, due to the ionically/electronically conductive network self-supported by the AEA cathode material, it can be combined with a high-capacity sulfur cathode to construct a hybrid S–LMS-based AEA cathode with high energy densities of over 770 W h kg^{-1} and 1900 W h L^{-1} at the electrode level. In the future, we believe that AEA electrodes will provide a new means of increasing the energy densities of batteries, regardless of the discovery of new materials. Furthermore, there is the possibility of increasing the energy density by exploring new AEA material candidates with a higher capacity and high voltage that effectively match the 4 V transition metal-oxide cathodes.

5. Experimental Section

Preparation of AEA Cathode: Mo_6S_8 was synthesized by methods previously reported. TiS_2 (99.9%), S_8 (99.95%, Innochem), $Li_4Ti_5O_{12}$ (99%), $Li_{10}GeP_2S_{12}$ (2–5 µm, Kejing star), Li_3PS_4 (2–5 µm, Kejing star), Li (99.95%, 80 µm, CEL), and In (99.999%, 30 µm) foils were obtained commercially. For LMS and LTS-based AEA cathode, the Mo_6S_8 and TiS_2 were used as the AEA electrode without further treatment. For hybrid S–LMS and LTO–LMS-based AEA cathode, S_8/Mo_6S_8 and $Li_4Ti_5O_{12}/Mo_6S_8$ were mixed in 32.5:67.5 by weight (162.5 mg, 337.5 mg,) and 40:60 by weight (200 mg, 300 mg). Then put them in an agate mortar for the ball-milling with 300 r, 12 h, and 300 r, 4 h to prepare the hybrid AEA cathode, respectively.

Batteries Assembly: The AEA-ASSLBs batteries were assembled by the configuration of AEA cathode/LGPS/Li_3PS_4/Li(In). A mass of 100 mg LGPS and 50 mg Li_3PS_4 SSE was uniaxially compressed at ≈216 MPa. Then the AEA cathode was added on top of the SSE and distributed homogenously and compressed at 360 MPa. A thickness of 80 µm Li foil was added (accompanying a 30 µm In foil, depending on the experimental designing.) The photography and schematic plot are shown in Figure S12, Supporting Information.

Characterization: The morphologies of the samples were investigated by SEM and TEM. The in situ XRD patterns of the all-solid-state battery were measured using Cu Kα radiation on an X-ray diffractometer from 29.8° to 37.5° (2θ), under 70 °C. The electrochemistry was conducted on a LAND battery test station at 70 °C. The electronic conductivities of the powder materials were measured by the 4-probe method at room temperature and atmosphere, and the Li-ion diffusion coefficient was measured by potentiostatic intermittent titration technique. More details of the materials and characterizations are provided in the Supporting Information.

Supporting Information

Supporting Information is available from the Wiley Online Library or from the author.

Acknowledgements

This work was supported by the Center for Clean Energy.

Conflict of Interest

The authors declare no conflict of interest.

Data Availability Statement

Research data are not shared.

Keywords

"all-electrochem-active" electrodes, all-solid-state batteries, conductive networks, energy density

Received: December 25, 2020
Revised: March 15, 2021

---

[1] J. M. Tarascon, M. Armand, *Nature* **2001**, *414*, 359.
[2] J. B. Goodenough, Y. Kim, *Chem. Mater.* **2010**, *22*, 587.
[3] T. T. Nagaura, *Prog. Batteries Sol. Cells* **1990**, *9*, 209.
[4] H. Li, *Joule* **2019**, *3*, 911.
[5] X. Wang, Y. L. Ding, Y. P. Deng, Z. Chen, *Adv. Energy Mater.* **2020**, *10*, 1903864.
[6] J. Janek, W. G. Zeier, *Nat. Energy* **2016**, *1*, 16141.
[7] B. J. Landi, M. J. Ganter, C. D. Cress, R. A. DiLeo, R. P. Raffaelle, *Energy Environ. Sci.* **2009**, *2*, 638.
[8] H. Zheng, R. Yang, G. Liu, X. Song, V. S. Battaglia, *J. Phys. Chem. C* **2012**, *116*, 4875.
[9] W. Xu, J. Wang, F. Ding, X. Chen, E. Nasybulin, Y. Zhangad, J. Zhang, *Energy Environ. Sci.* **2014**, *7*, 513.
[10] X. Shen, H. Liu, X. B. Cheng, C. Yan, J. Q. Huang, *Energy Storage Mater.* **2018**, *12*, 161.
[11] B. Caglar, P. Fischer, P. Kauranen, M. Karttunen, P. Elsner, *J. Power Sources* **2014**, *256*, 88.
[12] J. Ni, Y. Li, *Adv. Energy Mater.* **2016**, *6*, 1600278.
[13] S. Indris, R. Heinzmann, M. Schulz, A. Hofmann, *J. Electrochem. Soc.* **2014**, *161*, A2036.
[14] S. G. Stewart, J. Newman, *J. Electrochem. Soc.* **2008**, *155*, F13.
[15] W. Bauer, D. Nötzel, V. Wenzel, H. Nirschl, *J. Power Sources* **2015**, *288*, 359.
[16] N. Besnard, A. Etiemble, T. Douillard, O. Dubrunfaut, P. T. Van, L. Gautier, S. Franger, J. C. Badot, E. Maire, B. Lestriez, *Adv. Energy Mater.* **2017**, *7*, 1602239.
[17] E. J. Berg, C. Villevieille, D. Streich, S. Trabesinger, P. Novák, *J. Electrochem. Soc.* **2015**, *162*, A2468.
[18] S. Skaarup, K. West, B. Z. Christiansen, *Solid State Ionics* **1988**, *28*, 975.
[19] L. Liu, J. Xu, S. Wang, F. Wu, H. Li, L. Chen, *eTransportation* **2019**, *1*, 100010.
[20] R. Xu, J. Yue, S. Liu, J. Tu, F. Han, P. Liu, *ACS Energy Lett.* **2019**, *4*, 1073.
[21] Y. G. Lee, S. Fujiki, C. Jung, N. Suzuki, N. Yashiro, R. Omoda, D. S. Ko, T. Shiratsuchi, T. Sugimoto, S. Ryu. J. H. Ku, T. Watanabe, Y. Park, Y. Aihara, D. I. T. Han, *Nat. Energy* **2020**, *5*, 299.
[22] Z. Wan, D. Lei, W. Yang, C. Liu, K. Shi, X. Hao, L. Shen, W. Lv, B. Li, Q. H. Yang, F. Kang, Y. B. He, *Adv. Funct. Mater.* **2019**, *29*, 1805301.
[23] H. Bockholt, M. Indrikova, A. Netz, F. Golks, A. Kwade, *J. Power Sources* **2016**, *325*, 140.
[24] Y. H. Chen, C. W. Wang, X. Zhang, A. M. Sastry, *J. Power Sources* **2010**, *195*, 2851.
[25] A. J. Vaccaro, T. Palanisamy, R. L. Kerr, J. T. Maloy, *Solid State Ionics* **1981**, *2*, 337.
[26] M. Pan, T. Hakari, A. Sakuda, A. Hayashi, Y. Suginaka, S. Mori, M. Tatsumisago, *Electrochemistry* **2018**, *86*, 175.
[27] M. Mao, Z. Lin, Y. Tong, J. Yue, C. Zhao, J. Lu, Q. Zhang, L. Gu, L. Suo, Y. Hu, H. Li, X. Huang, L. Chen, *ACS Nano* **2020**, *14*, 1102.

[28] T. Yamada, S. Ito, R. Omoda, T. Watanabe, Y. Aihara, M. Agostini, U. Ulissi, J. Hassoun, B. Scrosatic, *J. Electrochem. Soc.* **2015**, *162*, A646.

[29] T. Matsuyama, A. Hayashi, C. J. Hart, L. F. Nazar, M. Tatsumisago, *J. Electrochem. Soc.* **2016**, *163*, A1730.

[30] A. L. Santhosha, N. Nazer, R. Koerver, S. Randau, F. H. Richter, D. A. Weber, J. Kulisch, T. Adermann, J. Janek, P. Adelhelm, *Adv. Energy Mater.* **2020**, *10*, 2002394.

[31] T. Matsuyama, M. Deguchi, K. Mitsuhara, T. Oht, T. Mori, Y. Orikasa, Y. Uchimoto, Y. Kowada, A. Hayashi, M. Tatsumisago, *J. Power Sources* **2016**, *313*, 104.

[32] A. Sakuda, N. Taguchi, T. Takeuchi, K. Tatsumi, Z. Ogumi, *Solid State Ionics* **2014**, *262*, 143.

[33] M. Nagao, H. Kitaura, A. Hayashi, M. Tatsumisago, *J. Electrochem. Soc.* **2013**, *160*, A819.

[34] S. R. Narayanan, D. H. Shen, S. Surampudi, A. I. Attia, G. Halpert, *J. Electrochem. Soc.* **1993**, *140*, 1854.

[35] W. Xue, Z. Shi, L. Suo, C. Wang, Z. Wang, H. Wang, K. P. So, A. Maurano, D. Yu, Y, C. , L. Qie, Z. Zhu, G. Xu, J. Kong, J. Li, *Nat. Energy* **2019**, *4*, 374.

[36] Y. Zhu, Y. Xu, Y. Liu, C. Luo, C. Wang, *Nanoscale* **2013**, *5*, 780.

[37] S. Wenzel. S. Randau, T. Leichtwei, D. A. Weber, J. Sann, W. G. Zeier, J. Janek, *Chem. Mater.* **2016**, *28*, 2400.

[38] J. Mao, K. Dai, M. Xuan, G. Shao, R. Qiao, W. Yang, V. S. Battaglia, G. Liu, *ACS Appl. Mater. Interfaces* **2016**, *8*, 9116.

[39] D.-K. Kim, H.-M. Park, S.-J. Jung, Y. U. Jeong, J.-H. Lee, J.-J. Kim, *J. Power Sources* **2006**, *159*, 237.

[40] S. R. Das, S. B. Majumder, R. S. Katiyar, *J. Power Sources* **2005**, *139*, 261.

[41] S. Y. Luchkin, K. Romanyuk, M. Ivanov, A. L. Kholkin, *J. Appl. Phys.* **2015**, *118*, 072016.

[42] R. Fallahzadeh, N. Farhadian, *Solid State Ionics* **2015**, *280*, 10.

[43] Z. Zhang, Y. Shao, B. Lotsch, Y. Hu, H. Li, J. Janek, L. F. Nazar, C. Nan, J. Maier, M. Armand, L. Chen, *Energy Environ. Sci.* **2018**, *11*, 1945.

[44] S. Cui, Y. Wei, T. Liu, W. Deng, Z. Hu, Y. Su, H. Li, M. Li, H. Guo, Y. Duan, W. Wang, M. Rao, J.Zheng, X. W. , F. Pan, *Adv. Energy Mater.* **2016**, *6*, 1501309.

[45] W. Li, K. Wang, S. Cheng, K. Jiang, *Adv. Energy Mater.* **2019**, *9*, 1900993.

[46] X. Yao, N. Huang, F. Han, Q. Zhang, H. Wan, J. P. Mwizerwa, C. Wang, X. Xu, *Adv. Energy Mater.* **2017**, *7*, 1602923.

[47] A. Van der Ven, J. Bhattacharya, A. A. Belak, *Acc. Chem. Res.* **2013**, *46*, 1216.

[48] H. Huo, J. Liang, N. Zhao, X. Li, X. Lin, Y. Zhao, K. Adair, R. Li, X. Guo, X. Sun, *ACS Energy Lett.* **2020**, *5*, 2156.

[49] P. G. Bruce, S. A. Freunberger, L. J. Hardwick, J. M. Tarascon, *Nat. Mater.* **2012**, *11*, 19.

[50] H. Qu, J. Zhang, A. Du, B. Chen, J. Chai, N. Xue, L. Wang, L. Qiao, C. Wang, X. Zang, J. Yang, X. Wang, G. Cui, *Adv. Sci.* **2018**, *5*, 1700503.

[51] Y. Liu, P. He, H. Zhou, *Adv. Energy Mater.* **2018**, *8*, 1701602.